Regular Article – Ultraintense and Ultrashort Laser Fields

Linear dichroism in few-photon ionization of laser-dressed helium

Severin Meister[1,a] , Aaron Bondy[2,3], Kirsten Schnorr[4], Sven Augustin[4], Hannes Lindenblatt[1], Florian Trost[1], Xinhua Xie[4], Markus Braune[5], Bastian Manschwetus[5], Nora Schirmel[5], Harald Redlin[5], Nicolas Douguet[6], Thomas Pfeifer[1], Klaus Bartschat[2], and Robert Moshammer[1]

[1] Max-Planck-Institute for Nuclear Physics, 69117 Heidelberg, Germany
[2] Department of Physics and Astronomy, Drake University, Des Moines, IA 50311, USA
[3] Department of Physics, University of Windsor, Windsor, ON N9B 3P4, Canada
[4] Paul Scherrer Institute, 5232 Villigen, Switzerland
[5] Deutsches Elektronen-Synchrotron, 22607 Hamburg, Germany
[6] Department of Physics, Kennesaw State University, Marietta, GA 30060, USA

Abstract. Ionization of laser-dressed atomic helium is investigated with focus on photoelectron angular distributions stemming from two-color multi-photon excited states. The experiment combines extreme ultraviolet (XUV) with infrared (IR) radiation, while the relative polarization and the temporal delay between the pulses can be varied. By means of an XUV photon energy scan over several electronvolts, we get access to excited states in the dressed atom exhibiting various binding energies, angular momenta, and magnetic quantum numbers. Furthermore, varying the relative polarization is employed as a handle to switch on and off the population of certain states that are only accessible by two-photon excitation. In this way, photoemission can be suppressed for specific XUV photon energies. Additionally, we investigate the dependence of the photoelectron angular distributions on the IR laser intensity. At our higher IR intensities, we start leaving the simple multi-photon ionization regime. The interpretation of the experimental results is supported by numerically solving the time-dependent Schrödinger equation in a single-active-electron approximation.

1 Introduction

The fundamental interaction of photons and matter is omnipresent in nature. Scientists not only employ light to investigate matter to high precision, but also as a tool to modify it in a well-controlled manner. The continuous development and optimization of light sources and combining them in a variety of ways makes it possible to enter unprecedented realms in light–matter interaction. For example, intense infrared (IR) pulses focused into a gas target can trigger high-harmonic generation of extreme ultraviolet (XUV) photons [1,2]. The two intrinsically synchronized radiation fields can be used in a variety of experiments on atoms and molecules. The scheme of XUV excitation and subsequent IR ionization is employed in photoelectron measurements to determine angular-distribution parameters, relative population strengths, and delay-dependent ionization yields [3–6]. Complementary transient absorption measurements employed an energetically broad XUV spectrum in combination with the IR driving laser and revealed light-induced states (LIS) in helium [7]. These LIS

can be attributed to two-color multiphoton excitation, allowing transitions beyond the one-photon electric-dipole selection rules. LIS were investigated in the context of transient absorption (see [8] for a review) with regard to their intensity dependence [9], quantum interference [10,11], and also for molecules [12]. Reduzzi *et al.* [13] brought up the aspect of polarization control, as the population of LIS depends on the relative orientation of the laser polarizations. We note that apart from the transient absorption context these states are dubbed dark states, as they are not accessible by single-photon absorption. In the following we will refer to the basic helium eigenstates, but the notation obviously depends on the viewing angle.

XUV-IR photoelectron measurements employing synchrotron [14] or free-electron laser (FEL) [15] radiation in combination with an IR laser have also been reported. These experiments, however, focused on photoelectron angular distributions (PADs) stemming from single-photon excited states. Building upon our earlier work on photoelectron yields originating from multiphoton excited states [16], the present study comprises a detailed analysis by employing multi-dimensional data sets. Here, we focus on polarization-

[a] e-mail: severin.meister@mpi-hd.mpg.de (corresponding author)

dependent or dichroic effects of PADs and their laser-intensity dependence.

The measurement employs FEL-XUV radiation in combination with a synchronized IR laser. Both sources are linearly polarized with adjustable orientation relative to each other. For temporally separate (non-overlapping) pulses, the preceding XUV pulse excites the helium atom to specific $(1snp)^1P$ states, while the delayed IR pulse ionizes the excited atom. For parallel orientation of polarizations and pulses in temporal overlap however, helium can be excited from its $(1s^2)^1S$ ground state to $(1sns)^1S$ and $(1snd)^1D$ states by simultaneous two-photon XUV-IR excitation. By absorbing additional IR photons, the excited atom can be ionized while details of the excited state can be inferred from the angular distribution and the kinetic energy of the emitted electrons. Measured PADs resemble hydrogen orbitals with varying angular momentum ℓ but conserved magnetic quantum number $m = 0$. For orthogonal orientation of the polarization axes, the PAD is altered fundamentally. The axial symmetry of the PAD along the polarization axis is broken, as the magnetic quantum number is $m = \pm 1$ with the IR defining the quantization axis. Furthermore, in this configuration excitation of ^1S states is completely suppressed, as predicted by selection rules for two-photon excitation [17]. Along with excitation, photoionization is suppressed at specific XUV energies, as the resonance enhancement is not available anymore.

We also report on a multiphoton feature just below the $(1s2p)^1P$ resonance involving excitation by one XUV and two IR photons. The analysis of the PADs allows to infer the excitation mechanism and an assignment to the $(1s4f)^1F$ resonance.

Moreover, the IR intensity dependence of PADs is analyzed. Since the XUV pulse deposits most of the required excitation energy into the helium, IR ionization of excited states can be studied at lower laser intensities than in a single-color experiment. Our analysis suggests that the simple multi-photon description is valid except for high IR intensities, as our high-intensity data set shows. Finally, the interpretation of our experimental results is supported by numerical solutions of the time-dependent Schrödinger equation (TDSE) in the single-active electron (SAE) approximation.

This manuscript is organized as follows. Section 2 provides a summary of the experimental (Sect. 2.1) and theoretical (Sect. 2.2) methods. Our results are presented in Sect. 3, separated for ionization via the $(1s3d)^1D$ and $(1s2s)^1S$ excited states 3.1, the $(1s4f)^1F$ excited state 3.2, and the IR intensity dependence of the PADs 3.3. A summary is given in Sect. 4.

2 Methods

2.1 Experimental Setup

The experiment was carried out with the reaction microscope (REMI) endstation [18,19] at the free-electron laser in Hamburg (FLASH2) [20,21] and a short-pulse IR laser based on optical parametric chirped-pulse amplification (OPCPA) [22]. The wavelength tunability of FLASH2 [23] was employed by scanning the XUV photon energy between 20.4 eV and 23.2 eV in steps of 0.1 eV with a bandwidth of 0.2 eV full-width at half maximum (FWHM). The FEL pulse duration was estimated to be about 40 fs FWHM in intensity and the FEL pulse energy was reduced to < 10 nJ, a level where two-XUV-photon absorption is suppressed. The IR laser was stretched to pulse durations of 90 fs (FWHM) to maintain, temporal overlap with the XUV pulses despite the timing jitter of several ten femtoseconds. The IR focal spot diameter of about 30 μm is significantly larger than the FEL focus (≈ 10 μm) and reached an intensity on the order of 10^{12} W/cm^2. The effective repetition rate in the measurement was 500 Hz.

The IR and FEL pulses enter the REMI collinearly while their foci overlap in the REMI center. Both the XUV and the IR radiation are linearly polarized, and the IR polarization can be rotated with respect to XUV polarization. A dilute supersonic gas jet of atomic helium crosses the laser foci, triggering single photoionization events. Charged fragments are separated by a homogeneous electric field and guided onto two time- and position-sensitive detectors. In order to achieve high momentum resolution, we selected a low electric field strength of 1.2 V/cm. A magnetic field, collinear with the electric field, forces charged particles on spiral trajectories ensuring a detection in the entire solid angle of 4π [24]. The chosen settings allow a 4π detection of electrons with kinetic energy up to 5 eV. Time-of-flight and position information is used to retrieve the particles' momentum vectors at the time of emission. Imposing momentum conservation on ions and electrons produced during the same laser pulse makes it possible to sort out fragments stemming from the same parent particle.

2.2 TDSE Calculation

The theoretical part of this study is based on numerically solving the TDSE in the SAE approximation. Although the model was described already in [16], we repeat it here for completeness and describe the extensions to implement the polarization. The ground state is effectively described as a $(1s1s')^1S$ state, where the $1s$ is close to the He$^+$ orbital and the $1s'$ is treated like a valence orbital, similar to the $n\ell$ orbitals in all the other $1sn\ell$ Rydberg states. As always in theory, the binding energies of the $n\ell$ valence electrons are not exact (see Fig. 1 for a quantitative overview), especially since we used a single-electron model potential rather than fully accounting for the electron-electron interaction and correlation in an *ab initio* manner. While $1sn\ell$ Rydberg states with orbital angular momenta $\ell \geq 2$ have very accurate binding energies, this is not quite the case for p electrons and particularly for s electrons, due to the small or missing centrifugal barrier. Since excita-
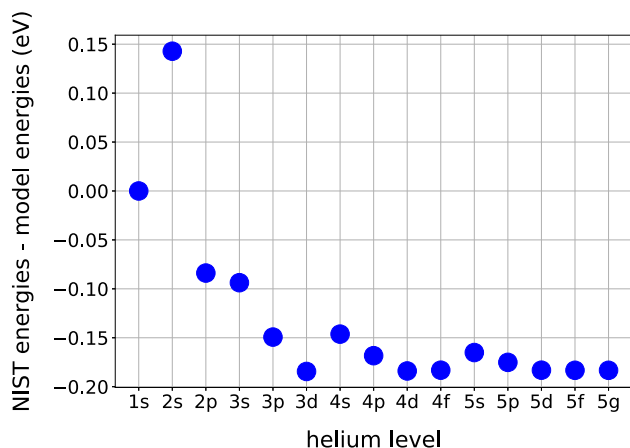
Fig. 1 Comparison of helium excitation energies between NIST [25] and the model of this study. With the ground state set at 0.00 eV, this indicates that the excitation energy of the 2s state is underestimated, while all the other excitation energies are slightly overestimated

tion energies are measured from the ground state, much of the remaining discrepancies are due to the binding energy of the $1s'$ orbital.

Specifically, we used the one-electron potential,

$$V(r) = -\frac{1}{r} - \left(\frac{1}{r} + 1.3313\right) \exp(-3.0634\,r), \quad (1)$$

where r is the distance from the nucleus, to calculate the valence orbitals. The deviations in the excitation energies, compared to the recommended values from the NIST database [25], are less than 0.2 eV even in the worst-case scenario (see Fig. 1) and do not alter the essential conclusions presented below. In the following we will usually omit the inner 1s electron and the total spin state (it would be a singlet in the two-electron description) to simplify the notation. Doubly excited states are not accessible with the photon energies used in the present experiment, and spin-forbidden transitions (i.e., excitation of triplet states) are negligible.

The laser intensity was chosen according to the available knowledge regarding the actual experimental conditions. The XUV pulse duration was taken as 40 fs (FWHM value of a peak intensity of 10^{10} W/cm^2 with a Gaussian envelope) and the IR pulse duration as 80 fs (FWHM). While the XUV photon energy was varied over a range in steps of 0.05 eV, the central IR photon energy was held fixed at 1.55 eV (800 nm).

Due to the fact that the lasers are linearly polarized along different directions, the cylindrical symmetry of the problem that we could take advantage of in the previous work [16] is no longer valid. The complications, however, are manageable in a straightforward way by employing an updated version of the code described by Douguet et al. [26]. Specifically, we used the velocity gauge and a variable radial grid step starting at 0.1 a.u. near the nucleus and gradually increasing to 0.2 a.u. far away, where we only need to describe rel-
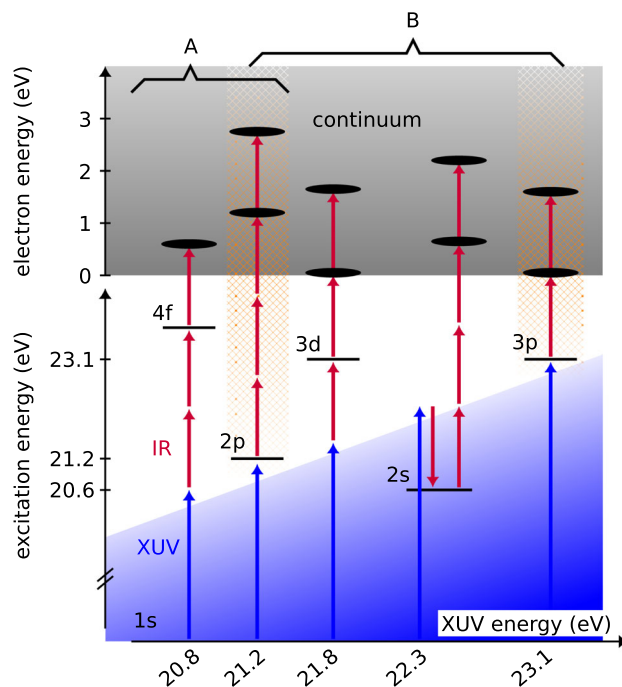

Fig. 2 Excitation and ionization scheme of the XUV energy scan in helium. For preceding XUV pulses there is only single XUV-photon absorption inducing p-state excitation (hatched orange region). For excitation into states with $\ell \neq 1$ a combination of an XUV photon and IR photons is required. Two-color multi-photon excitation is only possible for temporally overlapping pulses

atively slow electrons. The timestep was set constant at 0.05 a.u., partial waves up to $\ell_{max} = 12$ were coupled, and the numerical convergence of the predictions was checked by varying the parameters. Any apparent shortcomings of the theoretical results presented below are expected to be due to either the deficiency of the SAE model itself and/or the remaining uncertainties in the knowledge and, consequently, the description of the laser parameters.

3 Results and Discussion

3.1 Dichroism in Ionization via the 3d and 2s Excited States

A straightforward interpretation of the presented excitation and ionization mechanism is provided for XUV pulses preceding IR pulses. At matching XUV photon energies in the scanning range, the helium atom can be excited from the 1s ground state to np states. By absorbing additional photons of the moderately intense ($\approx 4 \times 10^{12}$ W/cm^2) delayed IR pulse, the excited atom can be ionized. The energy of the measured photoelectron depends on the binding potential of the excited state and the number of absorbed IR photons. Figure 2 shows schematically the underlying excitation and ion-
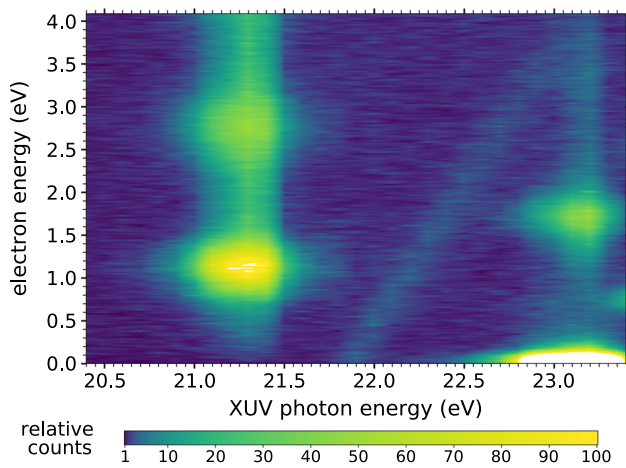
Fig. 3 Measured photoelectron yield as function of the photoelectron kinetic energy and XUV photon energy ($E\gamma$-plot) for preceding XUV pulses. At 21.2 eV (23.1 eV) the $2p$ ($3p$) state gets populated by the XUV. A subsequent IR pulse ionizes the excited atom. The emitted electrons appear as ATI peaks on the electron-energy axis. The diagonal line shows shakeup-ionization by the third harmonic of the FEL, leaving the He$^+$ in its first excited state

ization mechanism. The hatched regions in orange indicate the pathways that are accessible in the case of preceding XUV pulses. For example, the hatched region on the left shows ionization of helium via the $2p$ (21.2 eV) state. One XUV photon excites the atom to the $2p$ state and the additional absorption of at least three IR photons (1.55 eV each) from the delayed IR pulse results in ionization. The emitted photoelectron is detected and its measured kinetic energy can be reproduced by calculating the excess energy as follows:

$$E_{\text{XUV}}(21.2 \text{ eV}) + 3 \cdot E_{\text{IR}}(1.55 \text{ eV})$$
$$- I_{\text{p}}(24.6 \text{ eV}) = E_{\text{ele}}(1.2 \text{ eV}) \tag{2}$$

The atom can also absorb more photons than the minimum number required for ionization. The effect of above-threshold ionization (ATI) [27,28] manifests itself as regions of high yield separated by 1.55 eV in the electron energy.

The gray "continuum" region in the top of Fig. 2 illustrates the experimentally accessible part of the scheme. Respectively, Fig. 3 depicts the measured photoelectron yield as a function of the photoelectron kinetic energy and the scanned XUV photon energy ($E\gamma$-plot) for temporally delayed IR pulses. Here, the same XUV energy range as in Fig. 2 is depicted, while Fig. 4 and Sect. 3.2 will focus on regions B and A (cf. Fig. 2), respectively. According to the mechanism described, Fig. 3 shows a high yield of photoelectrons at XUV photon energies of the $2p$ (21.2 eV) and the $3p$ (23.1 eV) states. ATI peaks are found along the electron-energy axis, separated by the energy of one IR photon.

The diagonal line, starting at around 21.8 eV in Fig. 3, can be attributed to the third harmonic of the FEL. At this fundamental frequency, the third harmonic has an energy of 65.4 eV, just sufficient to ionize the helium atom ($I_{\text{p}} = 24.6$ eV) and leaving the He$^+$ ion in its first excited state ($n = 2$, 40.8 eV). The diagonal has a slope of three, as the photoelectron takes the excess energy.

For XUV and IR pulses in temporal overlap, the situation changes substantially, as various excitation pathways open up. In this case the helium atom is dressed in the IR radiation field during the XUV pulse and can absorb or emit IR photons, allowing access to transitions beyond the one-photon electric dipole selection rules. The simplest case of two-color two-photon excitation allows to couple the $1s$ ground state to ns and nd states. By absorbing additional IR photons, the excited atom can again get ionized, and the emitted photoelectron is measured.

In the case where both radiation fields are simultaneously present, all ionization pathways depicted in Fig. 2 are accessible. For excitation into the $3d$ state, the helium atom conjointly absorbs one XUV photon and one IR photon from the laser field. We also observe excitation into the $2s$ state, where conjointly to the XUV-photon absorption one IR photon is emitted to the laser field. As reported in reference [16], these two states dominate the light-induced features for the chosen IR and XUV parameters between the $2p$ and the $3p$ states. A detailed measurement in the XUV energy region B (cf. Fig. 2) is presented in Fig. 4. Subplot (a) is recorded for parallel polarization and shows two regions of high yield around 21.8 eV and 22.3 eV, which can be attributed to the $3d$ and the $2s$ states, respectively. The distribution of electron energies is broad due to the IR laser bandwidth and shortened lifetimes of the rapidly ionizing states. The broadness of the peaks along the XUV energy axis can be attributed to the XUV bandwidth and the AC Stark shift. The latter effect becomes
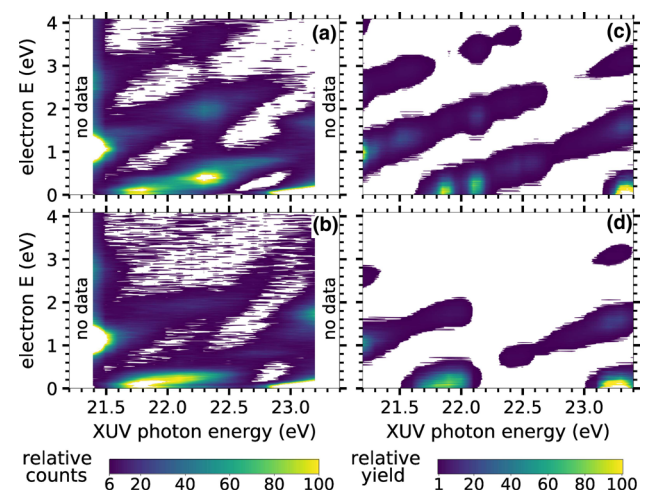

Fig. 4 $E\gamma$-plot of region B (cf. Fig. 2). Experiment: **a** parallel, **b** orthogonal polarization. Calculation: **c** parallel, **d** orthogonal polarization

even more pronounced as the timing jitter between pulses leads to varying IR intensities when the XUV pulses are present. This effect was accounted for in the TDSE calculation of Fig. 4c by summing over three IR intensities (1, 2 and 3×10^{12} W/cm²). Here, the two dominant multiphoton excitation features of the experiment are well reproduced, even though they are located at slightly different XUV photon energies. As mentioned in Sect. 2.2, the binding and, consequently, the excitation energies of our model deviate from the ones recommended by NIST. In fact our model underestimates the excitation energy of the $2s$ state and overestimates that of the $3d$ state, which explains the remaining differences between calculation and experiment.

Two-color multi-photon excitation includes the additional degree of freedom to change the relative orientation of the polarizations. By exploiting this handle, specific excitation pathways, and with it photoionization, can be deliberately suppressed. The measurement depicted in Fig. 4b is recorded with the same parameters as in (a), except for the orthogonal orientation of the polarization axes. While the $3d$ feature remains, the signal of the $2s$ state vanishes. This finding is predicted by the "two-photon electric-dipole selection rules" [17] for photons of differing frequency. According to this rule, the transition $\Delta J : 0 \rightarrow 0$ of the total electronic angular momentum is forbidden, while the magnetic quantum number m has to change by $\Delta m = \pm 1$. Since spin-flips during the excitation process are negligible, the ground-state spin (S = 0) is conserved and $L = J$.

The elongated region of high yield from the $3d$ state along the XUV photon-energy axis can be explained by the AC Stark shift. A pronounced shift of this state is described in Chen *et al.* [7] and Meister *et al.* [16]. In combination with the temporal jitter of the two radiation fields, it leads to the elongated feature. The calculated data for the orthogonal case are depicted in Fig. 4d. Similar to the experimental observation, the $2s$ state disappears while the $3d$ feature remains.

In addition to the kinetic energy of the photoelectrons, their angular distribution is measured. This allows us to deduce the quantum numbers of the excited state from which the electron was emitted. Figure 5 shows the measured three-dimensional photoelectron momentum distribution, which contains the PAD. Bins in momentum space are color-coded by the number of counts; each dot represents a photoelectron count. The two-dimensional plots on the walls depict the momentum distribution integrated along one axis.

Electrons in both subplots stem from the $3d$ resonance and were recorded at 21.8 eV XUV photon energy with their kinetic energy in the range from 0.07 eV to 0.16 eV. The weak contribution of the third harmonic is negligible and shows an isotropic PAD.

The PAD in Fig. 5a was measured for parallel polarization axes. In this configuration, each contributing photon changes the angular momentum by $\Delta \ell = \pm 1$ while the magnetic quantum number $m = 0$ is conserved from its ground-state value. The change of ℓ and m upon photon absorption is depicted in Fig. 6. For the measured "f-like" ($\ell = 3$) continuum distribution emission is found along the polarization axes and in two rings orthogonal to them. This suggests that the ionization proceeds via a d state.
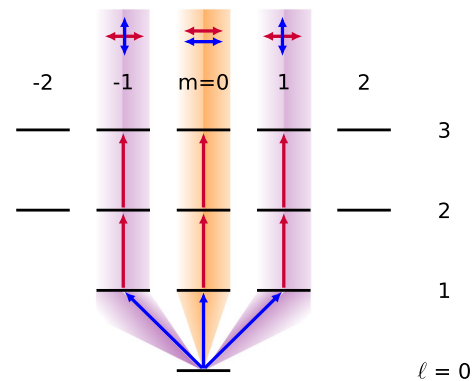

Fig. 6 Scheme of angular momentum ℓ and magnetic quantum number m upon multi-photon excitation. For XUV (blue) and IR (red) polarization parallel to each other, $\Delta m = 0$. For orthogonal orientation, $\Delta m = \pm 1$
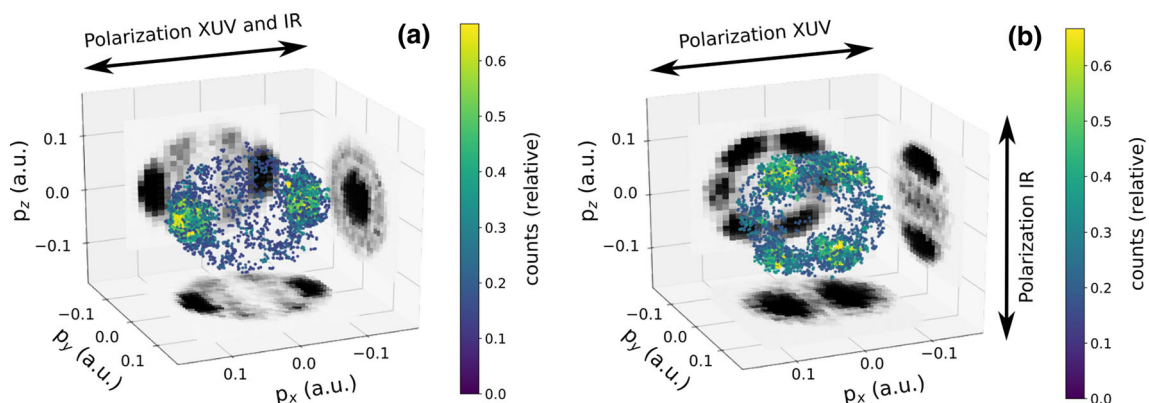

Fig. 5 Momentum distribution of photoelectrons stemming from the $3d$ LIS. The polarization axes of the XUV and IR are **a** parallel and **b** orthogonal to each other
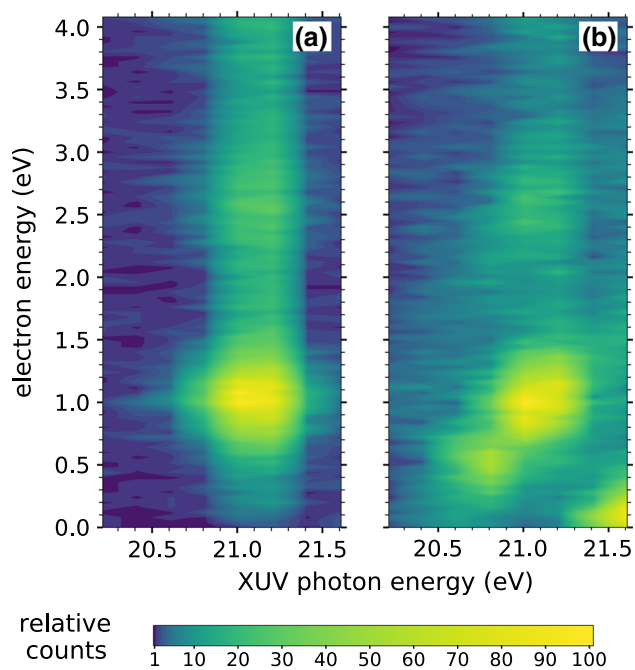
Fig. 7 Measured $E\gamma$-plot for region A (cf. Fig. 2) and parallel polarization. **a** Preceding XUV pulse, **b** temporal overlap. Ionization through a 2-IR-photon-coupled $4f$ state is observed at an XUV photon energy of 20.8 eV

Fig. 8 Photoelectron momentum distributions integrated along the laser propagation direction y for parallel polarization axes. The measured distributions are displayed in the top row, the calculated distributions in the bottom row

The PAD changes substantially in the case of orthogonal polarizations. The axial symmetry along the IR polarization is broken, and the distribution resembles that of a hydrogen orbital with $\ell = 3$ and $m = \pm 1$. This can be explained by taking the IR polarization as the quantization axis, so the linear polarization of the XUV is expressed as a superposition of right-hand and left-hand circularly polarized radiation fields. In this way, it is straightforward to see that the magnetic quantum number changes according to $\Delta m = \pm 1$ upon absorption of an XUV photon. The absorption of IR photons, on the other hand, does not change m. This is illustrated in Fig. 6.

3.2 Ionization via the 4f Excited State

For high IR intensities ($\approx 8 \times 10^{12}$ W/cm^2), we find a further peak at 20.8 eV, below the $2p$ resonance peak . A LIS for similar IR parameters in the same XUV energy range was observed by Chini *et al.* [10] in a transient-absorption (TA) measurement. It was tentatively assigned to excitation of np states by the absorption of one XUV photon and two IR photons. The present measurement however, suggests the feature to be a resonant enhancement of ionization via the $4f$ state as explained in the following.

Figure 7 shows an $E\gamma$-plot of region A (cf. Fig. 2) for parallel polarization axes. In subplot (a), the XUV pulse precedes the IR pulse, and thus ionization is restricted to resonant enhancement via p-state excitation. Within the depicted XUV energy range (scanned
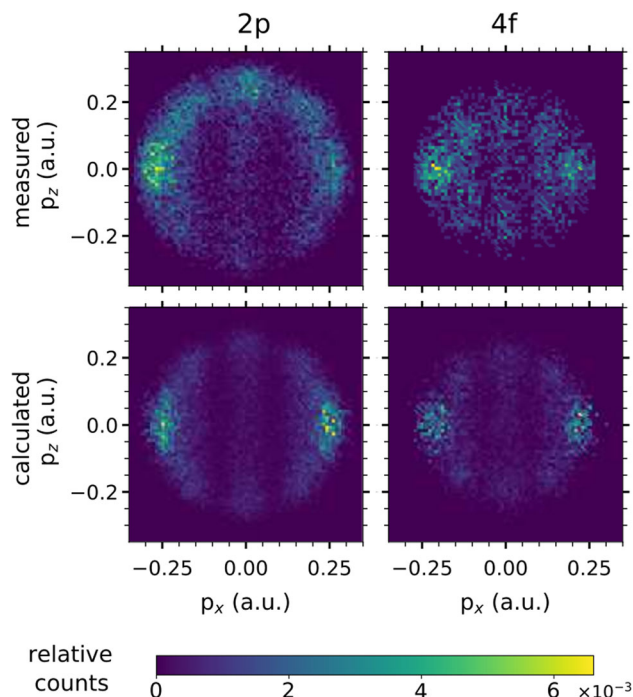
in 0.2 eV steps), there is only ionization via the $2p$ state at around 21.2 eV. The electron energy is about 1.2 eV, as the excited atom becomes ionized by absorbing three IR photons. This ionization pathway was previously described in Sect. 3.1 and is depicted in Fig. 2. For pulses in temporal overlap, the dressing IR-field opens up an additional excitation pathway. A new peak appears in Fig. 7b at slightly lower XUV photon energies and electron kinetic energies ($E_{\mathrm{XUV}} \approx 20.8$ eV, $E_{\mathrm{kin}} \approx 0.6$ eV) compared to the first ATI peak from the $2p$ state.

The following energetic considerations rule out certain excitation pathways and lead to the final assignment of the involved state. As the peak is only present for overlapping pulses, two-color excitation has to be considered. For excitation by one XUV photon plus one IR photon, even the lowest s and d states are out of reach (20.8 ± 1.55 eV) to be connected to the peak. The $2s$ (20.6 eV) state is too close to be populated, while the next $3s$ (22.9 eV) and $3d$ (23.1 eV) states are already too high to be populated. By considering an excitation involving absorption of one XUV photon plus two IR photons, there are nf and np states available. The angular momenta of the three photons either add up, changing the ground-state angular momentum by $\Delta \ell = +3$, or two angular momenta cancel each other resulting in $\Delta \ell = +1$. The case of negative $\Delta \ell$ is omitted, because the angular momentum of the helium ground state is already the lowest possible. The total available excitation energy is $E_{\mathrm{EXC}} = E_{\mathrm{XUV}}(20.8 \text{ eV}) + 2 \cdot E_{\mathrm{IR}}(1.55 \text{ eV}) = 23.9$ eV.

Possible excited states are $4p$ and $4f$, both with a binding energy of about 23.75 eV, and the $5p$ and $5f$ states, both with a binding energy of about 24.05 eV. In order to decide which states are more likely to be populated (either $n = 4$ or $n = 5$), we consider the AC Stark shift. To estimate the shift of these higher excited states, we take the shift between the $2p$ peak at 1.05 eV in Fig. 7b and the field-free value of Eq. 2 at 1.2 eV. By including the shift of about 0.15 eV, the binding energy of the $4p$ and $4f$ states is found at the matching excitation energy of 23.9 eV. This estimate is reasonable, as the highly excited states ($n = 4, 5$) experience a similar energetic shift with IR intensity as the continuum level. The possible resonances involved in the laser-dressing peak in Fig. 7b are narrowed down to the $4p$ and the $4f$ states.

The final identification is performed by analyzing the angular distribution of the photoelectrons stemming from the excited state. Figure 8 shows the measured and calculated photoelectron momentum distributions for parallel orientation of the polarization axes. The three-dimensional data are integrated along the mutual propagation direction y of the radiation fields and normalized to the total yield to provide a convenient comparison. The two plots in the upper row show the measured PAD of ionization through the $2p$ state and the nearby light-induced $4f$ state. In both cases emission is found along the polarization axis x and in three rings around the axes, appearing as three vertical lines. This distribution is "g-like" and corresponds to a continuum state with angular momentum $\ell = 4$. Consequently, this PAD pinpoints the excited state to be the $4f$ state rather than the $4p$ state, supported by monitoring the excited-state population during and after the pulse, which is possible in the calculation.

The two plots in the bottom row of Fig. 8 were generated by the numerical calculation described in Sect. 2.2. The electron kinetic energy was cut off at 1.8 eV to avoid an overlay of higher ATIs in the projection. The IR intensity was set to 3×10^{12} W/cm^2 and the XUV photon energy range was adapted to select the peak of interest. We introduced a Gaussian uncertainty in the electron energy of 0.2 eV to mimic the experimental conditions, including the IR bandwidth and the Stark broadening due to the temporal jitter between the pulses.

The $4f$ peak is also observed for orthogonal polarization axes. The measured $E\gamma$-plot in Fig. 9 samples region A (cf. Fig. 2) in steps of 0.1 eV. Similar to Fig. 7, subplot (a) is recorded for preceding XUV pulses, while (b) is recorded in temporal overlap. The peak appears at the same electron energy and XUV photon energy as in the case of parallel polarization.

Again, by analyzing the PAD of the peak, the ionization-enhancing resonance can be identified. Subplots in the top row of Fig. 10 depict the measured photoelectron momentum distribution for orthogonal polarization. In this case the magnetic quantum number increases to one, following the same argumentation as given in Sect. 3.1. Electrons are emitted in eight equally spaced solid-angle sections perpendicular to the
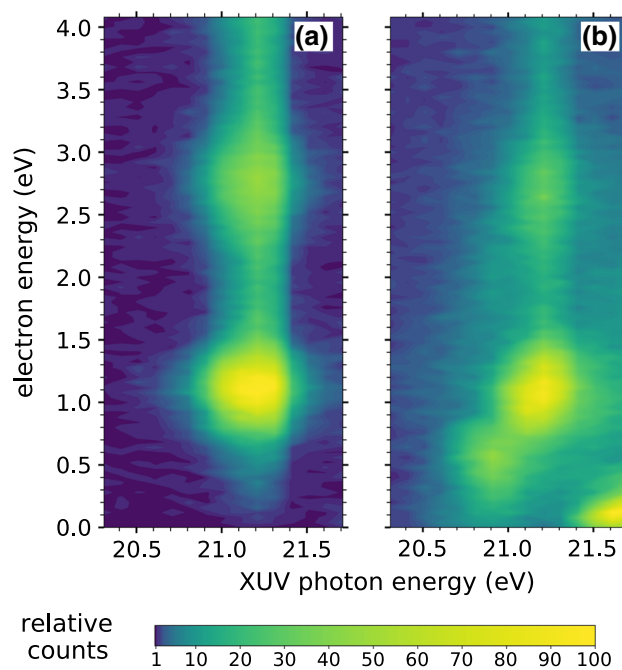

Fig. 9 Measured $E\gamma$-plot for region A (cf. Fig. 2) and orthogonal polarization. **a** Preceding XUV pulse, **b** temporal overlap. Ionization through a 2-IR-photon-coupled $4f$ state is observed at an XUV photon energy of 20.8 eV
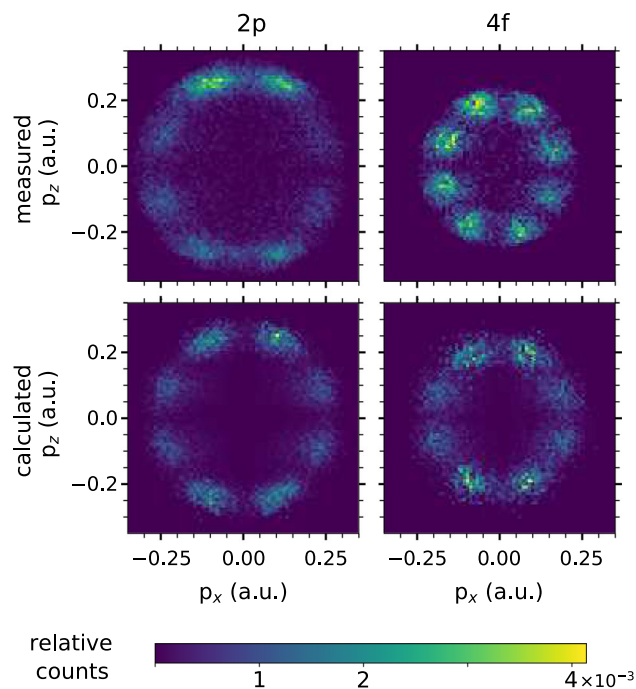

Fig. 10 Photoelectron momentum distributions integrated along the laser propagation direction y for orthogonal polarization axes. The measured distributions are displayed in the top row, the calculated distributions in the bottom row

laser propagation axis y. The node count corresponds to an $\ell = 4$ continuum state and, therefore, to an $\ell = 3$ excited f-state the electron was emitted from. There is good agreement in Fig. 10 between the experimental data in the top row and the theoretical predictions in the bottom row. Characteristics like the number of nodes and their relative intensity are reproduced as well as the diameter corresponding to the photoelectron kinetic energy.

3.3 IR Intensity Dependence of PADs

In the present XUV-IR scheme, the main energy contribution to ionization is provided by one XUV photon. This allows ionization of helium from excited states where electrons are less strongly bound. Electrons can be lifted over the remaining potential barrier by absorbing just a few additional IR photons, in contrast to ionization by an IR laser only, where strong fields are required. In the extreme case of tunnel ionization, electrons are predominantly emitted along the polarization axis, giving rise to the classical picture of electrons being accelerated along the electric field lines. On the contrary, at lower laser intensities within the multiphoton regime, complex PADs emerge, corresponding to discrete number of absorbed photons and angular momenta.

The present measurement exhibits PADs that indicate the photoionization process leaving the simple multi-photon regime. The Keldysh parameter γ [29] can be used to roughly quantify the localization within the continuous transition from the tunneling regime ($\gamma < 1$) to the multi-photon regime ($\gamma \gg 1$). The parameter is defined as

$$\gamma = \frac{\sqrt{2I_{\mathrm{p}}}\,\omega}{E_0}. \tag{3}$$

Here I_{p} is the ionization potential, ω the frequency, and E_0 the maximum field strength (all in atomic units). In the present experiment, helium is ionized from the $2p$ state, yielding $\gamma_{\mathrm{high}} = 1.9$ in the high IR intensity case ($\approx 8 \times 10^{12}$ W/cm^2) and $\gamma_{\mathrm{low}} = 5.3$ in the low IR intensity case ($\approx 1 \times 10^{12}$ W/cm^2). While γ_{low} is well within the multi-photon regime, γ_{high} enters the transition region.

Figure 11 shows calculated PADs for XUV and IR pulses in temporal overlap with parallel polarization axes. The angle Θ is defined as the angle between the polarization axis and the emission direction of the photoelectron. Photoelectrons in Fig. 11 are selected to cover the first ATI peak of ionization via the $2p$ state (XUV energy from 21.1 eV to 21.5 eV, electron energy from 0.6 eV to 1.4 eV). The data are normalized to the total integral yield. The number of maxima in Fig. 11 corresponds to the four absorbed photons (compare Fig. 2) and thus to the accumulated angular momentum. At low IR intensity, the PAD exhibits very pronounced minima and maxima, while at higher IR intensity the distribution changes distinctly. The minima at
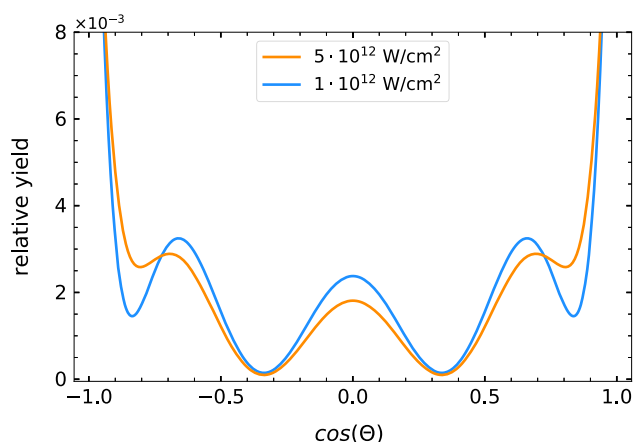

Fig. 11 Calculated PAD of the first ATI peak at 21.2 eV for temporal overlap and parallel polarization
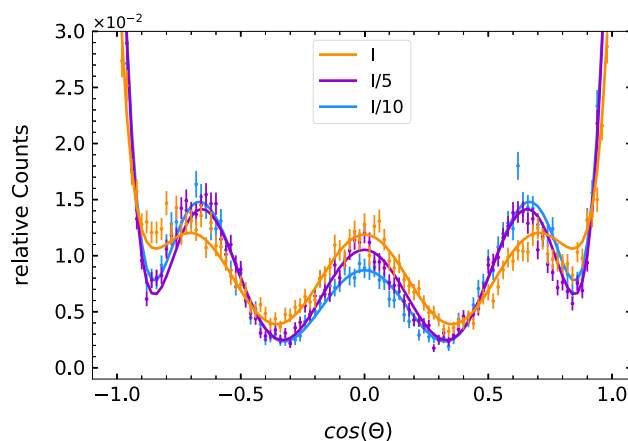

Fig. 12 Measured PAD according to Fig. 11. The selected electron energy range is 0.8 eV to 1.4 eV. The solid lines are fits to the data. See text for details

$\cos(\Theta) = \pm0.8$ smear out and the center maximum decreases. This trend can be regarded as the onset of the transition region to tunnel ionization, where emission is predominantly found along the polarization axis, where $\cos(\Theta) = \pm1$.

Corresponding to the calculation, Fig. 12 shows the measured PAD of electrons emitted from the first ATI at $E_{\mathrm{XUV}} \approx 21.2$ eV and $E_{\mathrm{kin}} \approx 1.2$ eV. Similar to theory, we find the PAD to change with IR intensity. This is not obvious in first place as the number of absorbed photons stays the same. The two minima around $\cos(\Theta) = \pm0.8$ smear out for increasing IR intensity, as predicted by the calculation. However, in contrast to theory, the center maximum increases in magnitude.

The solid lines in Fig. 12 depict fitted results to the data with their corresponding parameters listed in Table 1. The PAD can be described by the finite sum of even-rank Legendre polynomials P_n scaled with β_n

Table 1 Beta parameters of the fit in Fig. 12. All absolute errors $\leq \pm 0.05$

Int	β_2	β_4	β_6	β_8	β_{10}	β_{12}
I	0.83	0.75	0.18	**1.22**	-0.10	**0.10**
I/5	1.12	0.90	0.98	**1.95**	-0.22	**-0.02**
I/10	1.27	0.76	0.95	**1.85**	-0.16	**-0.09**

parameters [30,31]:

$$\frac{d\sigma}{d\Omega} = \frac{\sigma_0}{4\pi}\left(1 + \sum_{n\in\mathbb{N}} \beta_{2n} P_{2n}(\cos(\Theta))\right) \qquad (4)$$

Here σ_0 is the total emission cross section, and the angle Θ is defined as before. As explained in Ref. [5], the β_8 parameter corresponds to g-waves generated by four-photon absorption from the $\ell = 0$ ground state, which is dominating in the presented case. For high intensities β_8 decreases as well as lower order β-parameters (cf. Table 1). To explain the qualitative and quantitative observations at high IR intensities, mechanisms of higher order have to be considered. In the simplest case, the emitted electron can absorb one IR photon and emit one IR photon while conserving the photoelectron energy. The PAD, however, which reflects the angular momenta, is altered by this process. This is taken into account by extending the sum of equation 4 up to β_{12}, which allows to describe a six-photon process. However, the products $\beta_{2n}P_{2n}$ for different n are not disentangled, which makes a strict quantitative statement about the contribution of higher orders tentative.

Mayer *et al.* [5] investigated the laser-intensity dependence of PADs for similar parameters in an HHG-IR laser scheme. However, their findings are only comparable with ours to a limited extent, as the periodic HHG-based XUV spectrum couples to multiple excitation pathways.

An explanation for the slight discrepancy between theory and experiment (Figs. 11, 12), but also inconsistencies in Table 1, can be found in additional resonances being involved in the ionization process. The energy difference between the $2p$ state and higher-lying np states ($n = 6, 7, 8$) is about twice the IR photon energy. Theory might populate or miss some of these states due to its narrow IR bandwidth in contrast to experiment. Slight differences in resonance energies (imperfect model energies) and intensities (experimental temporal jitter) between the calculation and experiment lead to different contributions from the Rydberg np states, thus resulting in a discrepancy between the measured and calculated PADs.

4 Summary

We investigated photoelectron emission via excited states in laser-dressed atomic helium. The experimental results are in good agreement with TDSE calculations based on an SAE model. The simultaneous interplay of XUV and IR radiation enabled populating ^1S, ^1D and ^1F states, which are not accessible by single-photon absorption from the ground state. Two-color multiphoton excitation has an additional degree of freedom in the relative orientation of the polarizations. We analyzed the dichroic effect of different relative orientations on the PAD of electrons stemming from the $(1s3d)^1D$ state. For parallel orientation we found a PAD resembling a hydrogen orbital with $\ell = 3$ and $m = 0$, while for orthogonal orientation there is $\ell = 3$ and $m = \pm 1$. Furthermore, by changing the relative polarization direction, the photoionization signal can be suppressed at specific XUV energies. This can be explained by the fact that for orthogonal polarization axes the transition from the ^1S ground state to an ^1S excited state is forbidden by the two-photon selection rules, in contrast to the case of parallel polarization.

Finally, we investigated the IR laser intensity dependence of PADs obtained from photoelectrons of fixed energy. The electrons were emitted from the $2p$ state by the absorption of three IR-photons. At high IR intensities, we found the PAD to blur and higher-order terms to come into play. This observation can be regarded as the onset of the process to transit from the multiphoton to the tunneling regime.

Data availability statement This manuscript has no associated data or the data will not be deposited. [Authors' comment: The data to create the figures is available upon request.]

References

1. P.B. Corkum, Plasma perspective on strong field multiphoton ionization. Phys. Rev. Lett. **71**, 1994–1997 (1993)

2. M. Lewenstein, P. Balcou, M.Y. Ivanov, A. L'Huillier, P.B. Corkum, Theory of high-harmonic generation by low-frequency laser fields. Phys. Rev. A **49**, 2117–2132 (1994)

3. L.H. Haber, B. Doughty, S.R. Leone, Continuum phase shifts and partial cross sections for photoionization from excited states of atomic helium measured by high-order harmonic optical pump-probe velocity map imaging. Phys. Rev. A **79**, 031401 (2009)

4. P. Ranitovic, X.M. Tong, B. Gramkow, S. De, B. DePaola, K.P. Singh, W. Cao, M. Magrakvelidze, D. Ray, I. Bocharova, H. Mashiko, A. Sandhu, E. Gagnon, M.M. Murnane, H.C. Kapteyn, I. Litvinyuk, C.L. Cocke, IR-assisted ionization of helium by attosecond extreme ultraviolet radiation. New J. Phys. **12**(1), 013008 (2010)

5. N. Mayer, P. Peng, D.M. Villeneuve, S. Patchkovskii, M. Ivanov, O. Kornilov, M.J.J. Vrakking, H. Niikura, Population transfer to high angular momentum states in infrared-assisted XUV photoionization of helium. J. Phys. B Atomic Mol. Opt. Phys. **53**(16), 164003 (2020)

6. P. Johnsson, J. Mauritsson, T. Remetter, A. L'Huillier, K.J. Schafer, Attosecond control of ionization by wavepacket interference. Phys. Rev. Lett. **99**, 233001 (2007)

7. M. Shaohao Chen, J. Bell, A.R. Beck, H. Mashiko, W. Mengxi, A.N. Pfeiffer, M.B. Gaarde, D.M. Neumark, S.R. Leone, K.J. Schafer, Light-induced states in attosecond transient absorption spectra of laser-dressed helium. Phys. Rev. A **86**, 063408 (2012)

8. W. Mengxi, S. Chen, S. Camp, K.J. Schafer, M.B. Gaarde, Theory of strong-field attosecond transient absorption. J. Phys. B Atomic Mol. Opt. Phys. **49**(6), 062003 (2016)

9. M. Justine Bell, A.R. Beck, H. Mashiko, D.M. Neumark, S.R. Leone, Intensity dependence of light-induced states in transient absorption of laser-dressed helium measured with isolated attosecond pulses. J. Mod. Opt. **60**(17), 1506–1516 (2013)

10. M. Chini, X. Wang, W. Yan Cheng, D. Yi, D.A. Zhao, S.-I. Telnov, Z.C. Chu, Sub-cycle oscillations in virtual states brought to light. Scientific Reports **3**(1), 1105 (2013)

11. W.S. Chen, M.B. Mengxi, M. Gaarde, M.B. Schafer, Quantum interference in attosecond transient absorption of laser-dressed helium atoms. Phys. Rev. A **87**, 033408 (2013)

12. J.E. Bækhøj, L.B. Madsen, Light-induced structures in attosecond transient-absorption spectroscopy of molecules. Phys. Rev. A **92**, 023407 (2015)

13. M. Reduzzi, J. Hummert, A. Dubrouil, F. Calegari, M. Nisoli, F. Frassetto, L. Poletto, W. Shaohao Chen, M.B. Mengxi, K.S. Gaarde, G. Sansone, Polarization control of absorption of virtual dressed states in helium. Phys. Rev. A **92**, 033408 (2015)

14. P.O. Keeffe, A. Mihelič, P. Bolognesi, M. Žitnik, A. Moise, R. Richter, L. Avaldi, Near-threshold photoelectron angular distributions from two-photon resonant photoionization of he. New J. Phys. **15**(1), 013023 (2013)

15. S. Mondal, H. Fukuzawa, K. Motomura, T. Tachibana, K. Nagaya, T. Sakai, K. Matsunami, S. Yase, M. Yao, S. Wada, H. Hayashita, N. Saito, C. Callegari, K.C. Prince, P.O. Keeffe, P. Bolognesi, L. Avaldi, C. Miron, M. Nagasono, T. Togashi, M. Yabashi, K.L. Ishikawa, I.P. Sazhina, A.K. Kazansky, N.M. Kabachnik, K. Ueda, Photoelectron angular distributions in infrared one-photon and two-photon ionization of FEL-pumped rydberg states of helium. J. Phys. B Atomic. Mol. Opt. Phys. **46**(20), 205601 (2013)

16. S. Meister, A. Bondy, K. Schnorr, S. Augustin, H. Lindenblatt, F. Trost, X. Xie, M. Braune, R. Treusch, B. Manschwetus, N. Schirmel, H. Redlin, N. Douguet, T. Pfeifer, K. Bartschat, R. Moshammer, Photoelectron spectroscopy of laser-dressed atomic helium. Phys. Rev. A **102**, 062809 (2020)

17. K.D. Bonin, T.J. McIlrath, Two-photon electric-dipole selection rules. J. Opt. Soc. Am. B **1**(1), 52–55 (1984)

18. S. Meister, H. Lindenblatt, F. Trost, K. Schnorr, S. Augustin, M. Braune, R. Treusch, T. Pfeifer, R. Moshammer, Atomic, molecular and cluster science with the reaction microscope endstation at flash2. Appl. Sci. **10**, 2953 (2020)

19. G. Schmid, K. Schnorr, S. Augustin, S. Meister, H. Lindenblatt, F. Trost, Y. Liu, M. Braune, R. Treusch, C.D. Schröter, T. Pfeifer, R. Moshammer, Reaction microscope endstation at FLASH2. J. Synchrot. Rad. **26**(3), 854–867 (2019)

20. W. Ackermann, G. Asova, V. Ayvazyan, A. Azima, N. Baboi, J. Bähr, V. Balandin, B. Beutner, A. Brandt, A. Bolzmann, R. Brinkmann, O.I. Brovko, M. Castellano, P. Castro et al., Operation of a free-electron laser from the extreme ultraviolet to the water window. Nat. Photon. **1**(6), 336–342 (2007)

21. B. Faatz, E. Plönjes, S. Ackermann, A. Agababyan, V. Asgekar, V. Ayvazyan, S. Baark, N. Baboi, V. Balandin, N. von Bargen, Y. Bican, O. Bilani, J. Bödewadt, M. Böhnert, R. Böspflug, S. Bonfigt, H. Bolz, F. Borges, O. Borkenhagen, M. Brachmanski et al., Simultaneous operation of two soft x-ray free-electron lasers driven by one linear accelerator. New J. Phys. **18**(6), 062002 (2016)

22. T. Lang, S. Alisauskas, U. Große-Wortmann, T. Hülsenbusch, B. Manschwetus, C. Mohr, J. Müller,

F. Peters, N. Schirmel, S. Schulz, A. Swiderski, J. Zheng, I. Hartl. Versatile opcpa pump-probe laser system for the flash2 xuv fel beamline at desy, in *2019 Conference on Lasers and Electro-Optics Europe European Quantum Electronics Conference (CLEO/Europe-EQEC)*, p. 1 (2019)

23. B. Faatz, M. Braune, O. Hensler, K. Honkavaara, R. Kammering, M. Kuhlmann, E. Plönjes, J. Roensch-Schulenburg, E. Schneidmiller, S. Schreiber et al., The flash facility: advanced options for flash2 and future perspectives. Appl. Sci. **7**(11), 1114 (2017)

24. J. Ullrich, R. Moshammer, A. Dorn, R. Dörner, L. Ph, H. Schmidt, H. Schmidt-Böcking, Recoil-ion and electron momentum spectroscopy: reaction-microscopes. Reports Progr. Phys. **66**(9), 1463–1545 (2003)

25. A. Kramida, Yu. Ralchenko, J. Reader, and and NIST ASD Team. NIST Atomic Spectra Database (ver. 5.8), [Online]. https://physics.nist.gov/asd, January 14. National Institute of Standards and Technology, Gaithersburg, MD, p. 2020 (2021)

26. N. Douguet, A.N. Grum-Grzhimailo, E.V. Gryzlova, E.I. Staroselskaya, J. Venzke, K. Bartschat, Photoelectron angular distributions in bichromatic atomic ionization induced by circularly polarized vuv femtosecond pulses. Phys. Rev. A **93**, 033402 (2016)

27. P. Agostini, F. Fabre, G. Mainfray, G. Petite, N.K. Rahman, Free-free transitions following six-photon ionization of xenon atoms. Phys. Rev. Lett. **42**, 1127–1130 (1979)

28. Y. Gontier, M. Poirier, M. Trahin, Multiphoton absorptions above the ionisation threshold. J. Phys. B Atomic Mol. Phys. **13**(7), 1381–1387 (1980)

29. L.V. Keldysh, Ionization in the field of a strong electromagnetic wave. Sov. Phys. JETP. **20**, 1307–1314 (1965)

30. J. Cooper, R.N. Zare, Angular distribution of photoelectrons. J. Chem. Phys. **48**(2), 942–943 (1968)

31. L. Katharine, Reid, Photoelectron angular distributions. Ann. Rev. Phys. Chem. **54**(1), 397–424 (2003)